The Application of Scanning Transmission Electron Microscopy (STEM) to the Study of Nanoscale Systems

N.D. Browning, J.P. Buban, M. Chi, B. Gipson, M. Herrera, D.J. Masiel, S. Mehraeen, D.G. Morgan, N.L. Okamoto, Q.M. Ramasse, B.W. Reed, and H. Stahlberg

Abstract In this chapter, the basic principles of atomic resolution scanning transmission electron microscopy (STEM) will be described. Particular attention will be paid to the benefits of the incoherent Z-contrast imaging technique for structural determination and the benefits of aberration correction for improved spatial resolution and sensitivity in the acquired images. In addition, the effect that the increased beam current in aberration corrected systems has on electron beam-induced structural modifications of inorganic systems will be discussed.

N.D. Browning (✉)
Department of Chemical Engineering and Materials Science, University of California-Davis, One Shields Ave, Davis, CA 95618, USA

Department of Molecular and Cellular Biology, University of California-Davis, One Shields Ave, Davis, CA 95618, USA

Chemical and Materials Sciences Division, Pacific Northwest National Laboratory, 902 Battelle Boulevard, Richland, WA 99352, USA
e-mail: Nigel.Browning@pnnl.gov

J.P. Buban • S. Mehraeen
Department of Molecular and Cellular Biology, University of California-Davis, One Shields Ave, Davis, CA 95618, USA
e-mail: jpbuban@math.ucdavis.edu; smehraeen@ucdavis.edu

M. Chi
Materials Science Division, Oak Ridge National Laboratory, Oak Ridge, TN 37830, USA
e-mail: mchi@ornl.gov

B. Gipson • H. Stahlberg
C-CINA, Biozentrum, University Basel, WRO-1058 Mattenstrasse, CH-4058 Basel, Switzerland
e-mail: bryant.gipson@rice.edu; Henning.Stahlberg@unibas.ch

M. Herrera
Departamento de Ciencia de los Materiales e Ingeniería Metalurgica y Química Inorgánica, Facultad de Ciencias, Universidad de Cádiz, Pol. Rio San Pedro, 11510 Puerto Real (Cádiz), Spain
e-mail: miriam.herrera@uca.es

T. Vogt et al. (eds.), *Modeling Nanoscale Imaging in Electron Microscopy*, Nanostructure Science and Technology, DOI 10.1007/978-1-4614-2191-7_2,

Procedures for controlling the electron dose will be described along with image processing methods that enable quantified information to be extracted from STEM images. Several examples of the use of aberration-corrected STEM for the study of nanoscale systems will be presented; a quantification of vacancies in clathrate systems, a quantification of N doping in GaAs, a quantification of the size distribution in nanoparticle catalysts, and an observation of variability in dislocation core composition along a low-angle grain boundary in $SrTiO_3$. The potential for future standardized methods to reproducibly quantify structures determined by STEM and/or high-resolution TEM will also be discussed.

1 Introduction

Transmission electron microscopy (TEM) has long played a key role in driving our scientific understanding of extended defects and their control of the properties of materials—from the earliest TEM observations of dislocations [1] through to the current use of aberration-corrected TEMs to determine the atomic structure of grain boundaries [2]. With the current generation of aberration corrected and monochromated TEMs, we can now obtain images with a spatial resolution approaching 0.05 nm in both the plane-wave, phase-contrast TEM and the focused probe, Z-contrast scanning-TEM (STEM) modes of operation [3–5]. In addition to the increase in the spatial resolution, aberration correctors also provide an increase in the beam current and subsequently the signal-to-noise levels (contrast) in the acquired images. This means that small differences in structure and composition can be more readily observed and, for example, in the STEM mode of operation, complete 2-D atomic resolution elemental maps can be generated using electron energy loss spectroscopy (EELS) [6, 7]. Furthermore, the EEL spectra that are obtained using a monochromated microscope also show vast improvements over the spectra that could be obtained a few years ago—allowing bonding state changes to be observed from core-loss spectra with high precision [8] and the low-loss region

D.J. Masiel • D.G. Morgan
Department of Chemical Engineering and Materials Science, University of California-Davis, One Shields Ave, Davis, CA 95618, USA
e-mail: djmasiel@ucdavis.edu; dagmorga@indiana.edu

N.L. Okamoto
Department of Materials Science and Engineering, Kyoto University, Yoshida, Sakyo-ku, Kyoto 606–8501, Japan
e-mail: n.okamoto@at4.ecs.kyoto-u.ac.jp

B.W. Reed
Condensed Matter and Materials Division, Physical and Life Sciences Directorate, Lawrence Livermore National Laboratory, PO Box 808, Livermore, CA 94550, USA
e-mail: reed12@llnl.gov

Q.M. Ramasse
SuperSTEM Laboratory, J Block, STFC Daresbury, Daresbury WA4 4AD, UK
e-mail: qmramasse@superstem.org

of the spectrum to be used to map fluctuations in optical properties [9–11]. Taken all together, these newly developed capabilities for (S)TEM provide a comprehensive set of tools to measure, quantify, and understand the atomic scale properties of nanoscale materials, interfaces, and defects.

However, although the tools now exist to obtain very high-quality images from nanoscale materials, defects, and interfaces, as yet there has been very little work to quantify the information contained in them—other than to identify a structure and report composition variations in obvious cases across a hetero-interface. Images of individual interfaces, grain boundaries, or dislocations are typically presented as being "representative" of the whole structure with little proof that this is actually the case. In addition, the history of the sample is usually poorly defined in terms of its synthesis, preparation for the TEM, and beam irradiation history (which can easily have a significant effect on the structure, particularly when aberration-corrected microscopes are used). This is in stark contrast to the work that has been performed using TEMs for structural biology, where quantifying the information present in low-dose images has been the major emphasis of research for over 20 years [12–24]. Image processing and analysis methods for the study of organic systems can now routinely cope with variations across an image caused by sample movement and noise and can quantify the contribution of each—leading to a well-defined measurement of resolution and the accurate incorporation of these essential experimental factors into the structure determination procedure. In the case of the analysis of point defects in nanoscale systems, dislocations, grain boundaries, and interfaces by aberration-corrected (S)TEM, the lack or periodicity in the structure, large composition variations, and a sensitivity of the structure to beam modification actually make the experimental considerations very similar to those employed for organic systems. We can therefore use the image processing/analysis tools that have already been defined for structural biology to provide an unprecedented atomic scale characterization of nanoscale materials, defects, and interfaces—potentially even defining the effect of single atom composition variations on the structure and the subsequent properties.

2 Z-Contrast Imaging in STEM

The main principle behind the scanning transmission electron microscope is to use the electron lenses to form a small focused beam (probe) of electrons on the surface of the specimen [25] (Fig. 1a). As this electron probe is scanned across the surface of the specimen, the electrons that are scattered by the specimen are collected in a series of detectors that cover different angular ranges—the signal in each detector therefore contains a different part of the physics of the interaction of the beam with the specimen [26]. A 2-D image is created by displaying the output from one of these detectors as a function of the beam position as it is scanned across the specimen. Most STEM images use a high-angle annular dark field (HAADF) detector, in which the scattering that is collected is proportional to the Rutherford scattering cross-section that has a second power Z^2 dependence on the atomic number Z of the

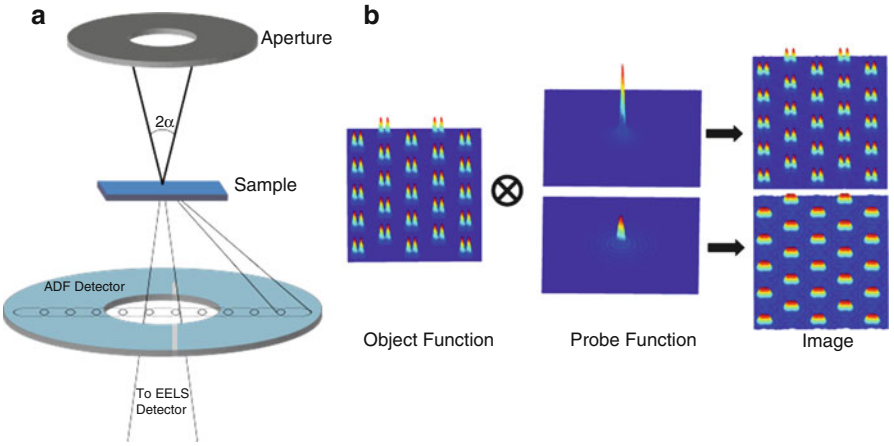

Fig. 1 (**a**) The geometry of the probe, detector and sample produce an overlapping CBED pattern at the detector plane. (**b**) The Z-contrast image (and electron energy loss spectrum) can, to a first approximation, be treated as a convolution between the probe intensity profile and the scattering cross section for the signal of interest (i.e. inelastic or elastic). The two probes shown illustrate the effect of aberration correction on the final image

scattering center—giving rise to the name Z-contrast imaging. From the earliest images of individual heavy atoms on a light support [25], the technique evolved to be able to image crystals with atomic spatial resolution [27]. In the remainder of this section, the principles behind the spatial resolution and the compositional sensitivity of the method will be described and the effect of aberration correction discussed.

2.1 Basic Concepts of Z-contrast Imaging

As described above, a Z-contrast image [27–32] is formed by collecting the high-angle scattering on an annular detector and synchronously displaying its integrated output on a TV screen or computer monitor while the electron probe is scanned across the specimen. Detecting the scattered intensity at high angles and integrating it over a large angular range effectively averages coherent effects between atomic columns in the specimen, allowing each atom to be considered to scatter independently with a cross-section approaching a Z^2 dependence on atomic number (Fig. 1b). This cross-section forms an object function that is strongly peaked at the atom sites. The detected intensity is, to a first approximation, a convolution of this object function with the probe *intensity* profile. The small width of the object function ($\sim$0.1 Å) means that the spatial resolution is limited only by the probe size of the microscope. For a crystalline material in a zone–axis orientation, where the atomic spacing is greater than the probe size ($\sim$0.1 nm for the JEOL 2100 C_s corrected STEM at UC-Davis, $\sim$0.1 nm for the Nion-corrected VG STEM at Lawrence Berkeley National Laboratory (LBNL), and 0.05–0.1 nm for the C_s

corrected FEI Titans at Lawrence Livermore National Laboratory (LLNL), LBNL, and Oak Ridge National Laboratory (ORNL)—these microscopes were used to obtain the results presented later in this chapter), the atomic columns can be illuminated individually. Therefore, as the probe is scanned over the specimen, an atomic resolution compositional map is generated in which the intensity depends on the average atomic number of the atoms in the column. An important feature of this method is that changes in focus and thickness do not cause contrast reversals in the image, so that atomic sites can be identified unambiguously during the experiment. As the images can be interpreted directly in real time while working on the microscope, they can be used to position the probe to obtain electron energy loss spectra from defined locations in the structure [33–39], thus permitting a full spectroscopic analysis to be correlated with the image on the atomic scale.

Since the initial development of the Z-contrast imaging technique, there have been many studies that have confirmed the general concept of incoherent imaging described above—in particular, identifying the location of atomic columns in the image is straightforward. However, interpretation of the intensities within the atomic columns seen in the images is a little more complicated than the simple incoherent model suggests [38–42]. If you want to interpret the absolute intensities in the individual columns in terms of the presence of vacancies and impurities, then first principles simulations of the atomic structures must be accompanied by image simulations—there are currently several available packages to perform these simulations [43,44]. As the aim of this chapter is to discuss the applications of quantitative imaging in STEM, we will not discuss the details of the simulations further here, other than to mention in the subsequent sections when simulations were used.

2.2 Aberration Correction

In conventional high-resolution TEM imaging and in atomic resolution Z-contrast imaging, the resolution of the final image is limited by the aberrations in the principal imaging lens. For STEM, this means the aberrations in the final probe-forming lens—which determines the spatial extent of the electron beam on the surface of the specimen. As with other high-resolution methods, defocus can be used to balance out the effects of aberrations up to some optimum value, usually called the Scherzer defocus, with a resolution given by

$$d = 0.43(C_s\lambda^3)^{\frac{1}{4}} \tag{1}$$

As can be seen from this equation, there are two principle factors that control resolution—the wavelength λ of the electrons (determined by the acceleration voltage of the microscope) and the spherical aberration coefficient C_s of the lens. For typical C_s values in uncorrected state-of-the-art 200 kV TEM/STEM microscopes ($C_s \approx 0.5$ mm), this gives an optimum probe size of $\sim$0.12nm [45]. This equation also shows the two methods that can increase the spatial resolution—higher voltage and lower C_s.

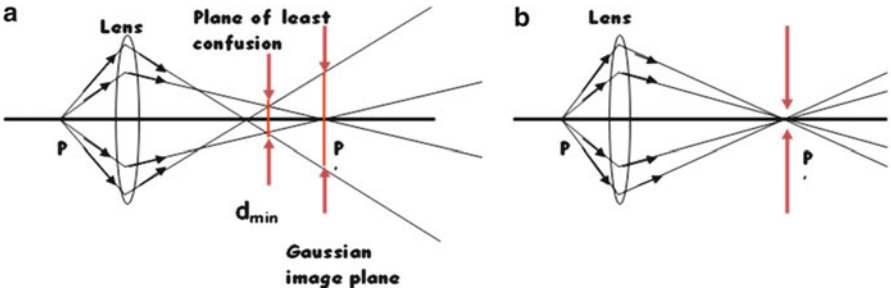

Fig. 2 The effect of spherical aberration (**a**) can be corrected to create a smaller, more intense electron probe (**b**)

In the late 1990s there were two main efforts underway to establish C_s correctors for TEM [3] and STEM [4]. For the formation of a STEM probe, the effect of C_s correction is shown schematically in Fig. 2. Practically the effect of C_s correction means that a larger area of the lens is free from spherical aberration, allowing larger apertures to be used and a higher resolution to be obtained [46]. An important corollary to the increase in spatial resolution is that the larger aperture size means that the smaller probe that is formed can have up to an order of magnitude more beam current than a conventional STEM probe [6]. Now that spherical aberration has essentially been removed as the limitation in the probe size, higher order aberrations are the limiting factors. As was the case with the Scherzer defocus, the aberration corrector can now be adjusted to compensate for those higher order aberrations by tuning C_s itself to an optimal value. Although due to the complexity of the multipole electron optics of correctors many more parameters actually control the probe size, (1) can be modified to yield the probe full-width-at-half-maximum ρ of a simplified system limited only by 5th order aberration C_5 [47]:

$$\rho = 0.37(C_5\lambda^5)^{\frac{1}{6}} \tag{2}$$

For a state-of-the-art aberration-corrected STEM, the probe size can now approach 0.05 nm [5] and designs are currently being implemented that should push resolution even further to $\sim$0.03 nm [48]. Aberration-corrected STEMs are now becoming the standard for high-resolution imaging, with many applications to solve materials science problems being present in the literature [49–53].

Another advantage of the aberration corrector for STEM is the increased usefulness of other imaging signals not traditionally exploited in scanning mode. Instead of the annular-shaped detector used for Z-contrast imaging, a detector placed directly on this axis will form a bright field image, which can be shown by simple optical reciprocity considerations to be equivalent to a conventional high-resolution TEM phase contrast image. Thanks to the larger aberration-free area of the electron wavefront, the collection angle for this bright field detector can be increased in a corrected instrument and high-quality images can be obtained [26]. As a supplement to the Z-contrast images described above, simultaneous phase-contrast images can

provide information on the location of light elements in the structure that are not imaged clearly by the Z-contrast technique. On the other hand, one issue that is brought up by the use of large apertures is the reduction in depth of focus, whereas in the analogous case of photography, for instance, where a very small depth of focus is highly sought after to produce pleasant out-of focus backgrounds with large aperture portrait lenses, it means in an aberration-corrected STEM that the coupling between the probe on the surface of the sample and the atomic columns is more complex. While this decrease in depth of focus can have a negative effect on high-resolution imaging, it has been proposed as a method to perform optical sectioning of samples to deliver 3-D imaging [54–57]. Although in the straight STEM approach (as opposed to the confocal approach), the 3-D images suffer from distortion due to the missing wedge of information (the same way that tilt tomography does [58,59]), it can have applications in the study of nanostructures [60].

2.3 Low-dose Imaging

As stated in the previous section, the increase in spatial resolution provided by aberration correctors is accompanied by an increase in the beam current. While there are materials that are still able to withstand the $>10^5\,e^-/Å^2$ dose that a typical aberration-corrected STEM image now contains, beam modification of the sample is now a significant issue for materials science. This is especially true when we start to consider what we would like to do with the aberration-corrected STEM. One of the big impacts that the increase in resolution and sensitivity can give us is the ability to look at interfaces and defects in more detail and to examine the distribution of point defects (vacancies and impurities) around these structures. However, point defects are mobile and by definition, the defect and interface structures are going to be less stable than the bulk material. To overcome some of the effects of beam damage, recent work in aberration-corrected STEM has moved to lower voltages. While this will significantly reduce the effects of knock-on damage, it does not tell the whole story of beam damage. Experience from the structural biology field shows that for organic systems, it is the electron dose that is the important thing, rather than the accelerating voltage. This implies that knock-on damage is not going to be the limitation for every materials system.

In the case of aberration-corrected TEM, high-resolution images of organic systems can be obtained by using the standard low-dose approach to imaging [61]. Applying a similar approach to STEM is not as straightforward, as the typical mechanism to reduce beam current is to change the parameters of the electron gun. However, this changes the electron optics in the column and leads to a misalignment of the corrector—which is then hard to realign under low-dose conditions as the auto tuning software typically requires high signal-to-noise images or diffractograms to converge accurately. Despite all of the problems, it is possible to control the dose in the aberration-corrected STEM to permit atomic scale images to be obtained of

beam sensitive materials [62], and to investigate where the resolution will be limited by dose [63].

Following the approach in [63], we discuss here briefly the effect of lowering the dose on STEM images. The images were acquired using a JEOL JEM-2100F/C_s STEM/TEM with a retrofitted CEOS C_s-corrector operating at 200 kV. After C_s-correction, the probe diameter was $\sim$0.1 nm. A reading of the electron beam current at normal operating conditions was measured at 50 pA using the ammeter behind the small phosphorus viewing screen. For conventional high-dose STEM operation, the JEM-2100F is typically operated with a gun extraction voltage (A1) of 2.8 to 3.2 kV, and an electrostatic gun lens voltage (A2) between 6.8 and 7.3 kV. To record images with a reduced beam current, A1 and A2 were reduced to 0.9 kV and 6.2 kV, respectively. Images were obtained using an annular dark-field (ADF) detector with an inner cutoff angle of $\sim$30 mrad, corresponding to low-angle annular dark-field (LAADF) imaging—here incoherence is sacrificed for more electrons reaching the detector. The Gatan Digiscan 688 system was used as the scan driver, which was controlled by the Gatan Digital Micrograph software package. Figure 3a shows an image of $SrTiO_3$ [001] taken under the typical high-dose imaging conditions described above. Here, the imaging conditions are a beam current of $\sim$50 pA, a pixel dwell time of 20 µs per pixel, and a pixel size of 0.05 Å^2. These imaging conditions correspond to a radiation dose of approximately 1.0×10^8 e$^-$/Å^2. As expected, the calculated power spectrum shows clearly visible diffraction spots at 1.3 Å resolution. However, the electron dose is approximately 10 million times too high for most biological specimens.

The most straightforward way to reduce the electron dose during image acquisition in STEM is to reduce the pixel dwell time (i.e., increasing the STEM scanning speed). The Gatan Digiscan system allows the dwell time to be reduced to a minimum of 0.5 µs per pixel. In the STEM, magnification corresponds to changing the pixel size. We chose a magnification to give a pixel size of 1.0 Å^2. Figure 3b shows an image of $SrTiO_3$ taken with a dwell time of 0.5 µs per pixel with a typical probe current of approximately 50 pA. The specimen is exposed to a total radiation dose estimated to be 150 e$^-$/Å^2. A close inspection of the image, however, reveals a streaking artifact parallel to the scan direction. The power spectrum and Fourier-filtered image are shown inset. Fourier filtering was done by masking the Fourier transform spots, using a mask size of 15 nm^{-1} and edge blurring of 5 pixels (1.0 nm^{-1}). Noticeable streaking is observed in the raw image, which influences the anisotropic background noise. This observed streaking artifact is caused by a slow reaction time of the photomultiplier/read-out electronics, which leads to an anisotropic smearing out of individual signal peaks. An additional artifact that contributes to the anisotropic background is a random horizontal offset of scan lines.

This streaking effect can be significantly reduced by increasing the dwell time, i.e., scanning slower. Using the JEOL JEM-2100F/C_s, the streaking effect was noticeably reduced when images were recorded with a dwell time of 2.0 µs per pixel. However, the fourfold increase in the dwell time would increase the electron dose from $\sim$450 e$^-$/Å^2 to $\sim$1,800 e$^-$/Å^2. Since beam sensitive specimens often

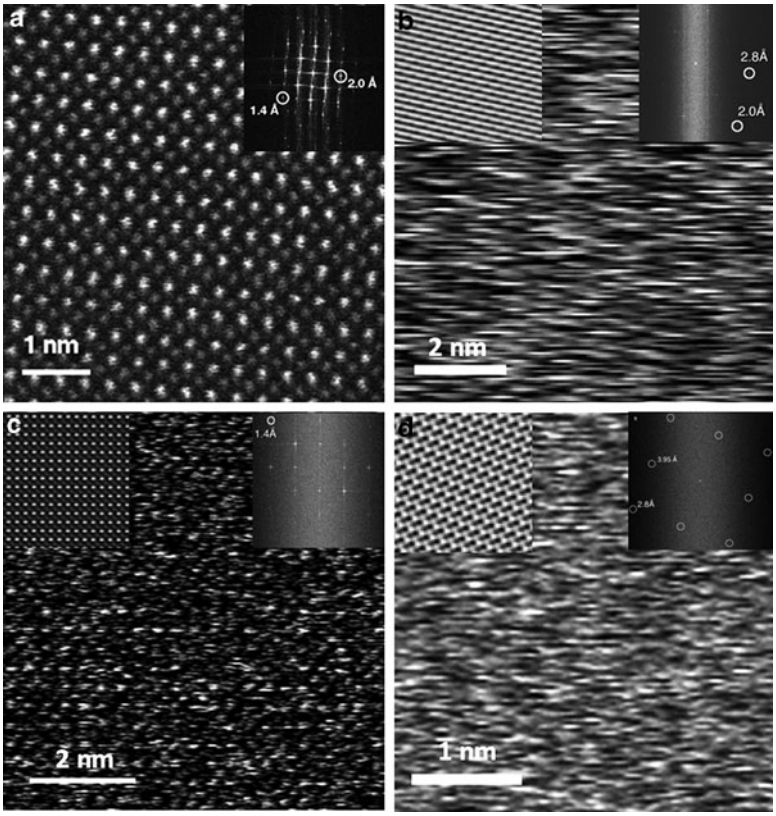

Fig. 3 Images of $SrTiO_3$ [001] (**a**) acquired with a C_s-corrected JEOL 2010F with a radiation dose of $\sim 5 \times 10^8\,e^-/Å^2$ (inset fourier transform shows reflections corresponding to a resolution of 1.3 Å). (**b**) Taken with a dwell time of 0.5 μs per pixel, a pixel size of 0.3 $Å^2$ and a typical gun current of approximately 50 pA, yielding an estimated radiation dose of $\sim 450\,e^-/Å^2$ (inset fourier transform/inverse transform show higher order reflections at 2.0 Å). (**c**) Taken with a dwell time of 2.0μs per pixel and pixel area of 0.1 $Å^2$, using a gun current of 4 pA, which gives a dose of $\sim 220\,e^-/Å^2$. The streaking effect is reduced in both the image and the inset fourier transform/inverse transform). (**d**) Obtained with 2% of the standard gun current with a pixel dwell time of 1.0 μs and pixel size of 0.4 $Å^2$. The dose is estimated to be $25\,e^-/Å^2$ (reflections at 2.7 Å with corresponding lattice fringes are seen in the fourier transform/inverse transform)

require imaging with much lower electron doses, additional dose reduction is required. We achieve this by decreasing the probe current. Figure 3c shows an image of $SrTiO_3$, that was recorded with a dwell time of 2.0 μs per pixel and a pixel size of 0.1 $Å^2$, while using a probe current of only $\sim 4\%$ of the current used for the image in Fig. 3a. The scan artifacts are noticeably less in both the image and the power spectrum and the apparent resolution is increased with only a small increase in the total electron dose, estimated to be $220\,e^-/Å^2$. Note that the orientation of the lattice

is at a significant angle to the scan direction in order to minimize potential artifacts in the Fourier transform due to periodicities induced by the scan lines. In the power spectrum, one can see spots at 1.3 Å, which is close to the expected resolution limit of 1.0 Å for the C_s-corrected JEOL 2100F/C_s.

Next, we reduced the electron dose to $\sim 15\,e^-/Å^2$ by lowering the probe current further to only $\sim 2\%$ of the probe current at full emission (corresponding to a current ~ 1 pA) and by decreasing the scan speed to 1.0 μs per pixel, and increasing the pixel size to $0.4\,Å^2$. An example image is shown in Fig. 3d. The SNR of the resulting real-space image is so low that the naked eye does not discern any structural information in this image. Nevertheless, near atomic resolution features can still be documented in the power spectrum and Fourier-filtered image. Spots at 3.95 Å and 2.7 Å can be clearly seen in the calculated power spectrum of the nonprocessed image. Increasing the scan speed to 2.0 μs per pixel (and consequently doubling the dose to $\sim 30\,e^-/Å^2$), the power spectrum of the recorded image showed clearly visible diffraction spots at 2.0 Å resolution. Lowering the probe current below 2% resulted in images that had no discernible features in the power spectrum.

The images shown in Fig. 3 demonstrate that it is still possible to get high resolution from aberration-corrected images even under low-dose conditions. While low dose is not necessary for all samples—the examples cited above demonstrate that for the right problem, aberration-corrected STEM gives beautiful images—it does mean that we can use it for problems that have so far been ignored because of the beam damage issue. Furthermore, the control of the dose described here is not the optimum approach. A far better approach would be to use a set of fast deflector plates to move the beam on/off the specimen to control the dose—thereby avoiding any change in the electron optics. Such a deflector system is already under development for the dynamic transmission electron microscope (DTEM) and its application to STEM should be straightforward [64].

3 Application to Nanoscale Systems

The STEM methods described above can be applied to any materials system. The information that can be obtained depends only on the signal to noise in the images that are obtained—essentially controlled by the ability of the sample to absorb electron dose without modifying the structure. In this section, a series of examples will be presented that show how the STEM methods can be applied to extract quantitative information from materials systems. In the first example from the study of clathrates, 2-D crystallography methods are used to understand and correct distortions in STEM images and then determine an average structure. In the second example, averaging methods are described that enables the effects of point defects on the structure to be observed. These effects are used to determine the formation of small clusters of impurities distributed in the bulk. The third example presents

an analysis of grain boundaries. In this case the symmetry of the structure is broken by the presence of grain boundary dislocations, limiting the use of crystallographic averaging methods. However, it is still possible to use multiple images of the grain boundary to infer details of statistical deviations in structure and composition in the dislocation core. The fourth and final example, describes a mathematical method to quantify the size of nanostructures to an accuracy of ~ 10 pm. The use of these methods either individually or in combination can provide unprecedented insights into the structural properties of nanoscale materials.

3.1 The Structure of Clathrates

As discussed above, zone axis Z-contrast images reveal the atomic structure of the sample with a resolution that is defined by the probe size of the microscope. In the aberration corrected microscopes that are now standard, this resolution can be on the subangstrom level and is typically accompanied by an increase in signal to noise—resulting in higher contrast images. However, in some cases the increase in beam current (that gives rise to the increase in signal to noise) results in beam damage to the sample. For each material being studied, there is therefore an optimum electron dose that does not modify the structure. For systems where this is a low number, the aberration-corrected images do not "look better" than conventional STEM images (and may even be worse) meaning that many of the benefits of the aberration corrector are lost. As there are many expectations among microscopists for aberration-corrected images, sometimes experimentalists push the beam current further than the damage limit to obtain the best looking images. While many of the published images may be truly "representative" of the structure, it is impossible to say for sure without an attempt to quantify the resolution under different beam conditions. Fortunately, in most experimental cases this is relatively straightforward to do, as the full images contain many subimages of the crystal unit cell and/or interface structure. The repetitive nature of these images allows standard image processing techniques that have been developed for electron crystallography of biological macromolecules (i.e., developed to extract the highest resolution information from the noisiest images) to be applied. These methods can be used to enhance the signal-to-noise present in the original images, to remove distortions in the images that arise from either the instrumentation or the specimen itself, and to quantify properties of the material in ways that are difficult without such data processing, i.e., the improved data from aberration-corrected microscopes can be recovered even from poorer quality low-dose conditions. Here this concept is demonstrated through the analysis of Si_{46} clathrate samples [65, 66].

The test images of the K_8Si_{46} clathrate have been obtained from a 100 kV Nion-corrected VG HB501 with nominal 0.1 nm probe size (Fig. 4a). Figure 4b shows the Fourier transform obtained after the image in (a) had been floated into a larger area that was filled with a constant gray level based on the average density value of the original image. The red and blue arrows marked in this panel indicate the

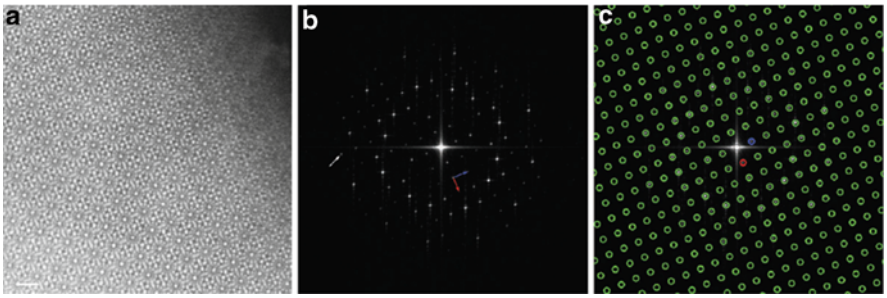

Fig. 4 (**a**) Z-Contrast image of K_8Si_{46}, (**b**) Fourier transform of the image and (**c**) the definition of the reciprocal lattice points used to construct the lattice. The *scale bar* in (**a**) represents 1.0 nm and the *white arrow* in (**b**) marks a reflection at 0.164 nm^{-1} resolution

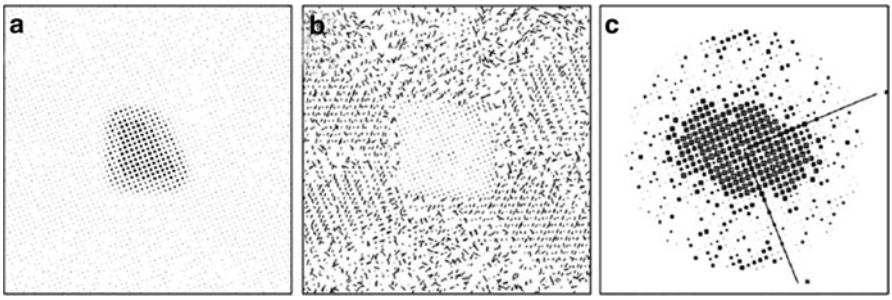

Fig. 5 (**a**) Unit cell locations, (**b**) distortion field, (**c**) reciprocal lattice from Fig. 4a

reciprocal space lattice vectors that describe the unit cell. Figure 4c is identical to (b), with the reciprocal space lattice points being marked using green circles. The red and blue circles nearest the origin of the Fourier transform respectively mark the positions of the (10) and (01) reflections that were used to build this lattice and that define the unit cell. Note that this lattice marks both the clearly visible diffraction spots and also extends the regions of the Fourier transform that appear featureless in this representation. The total number of possible lattice points in this Fourier transform is $>$2,600 while the number that fall within the default resolution limits of the microscope is only $\sim$1,000.

Having defined the image and Fourier transform of the image, standard processing techniques can then be applied. In Fig. 5, the unit cell locations and vector distortion field found during unbending and IQ plot of structure factors is shown. Figure 5a shows the location of unit cells found in the image created after floating Fig. 4a into a larger array for image processing. The size of the point marking each unit cell is related to the quality (IQ, or strength of the signal in the cross-correlation map) of the unit cell, with the largest points indicating the best locations. The best unit cell locations are limited to the region of the image that contains the image shown in Fig. 4a. Figure 5b shows the distortion field mapping the deviation between

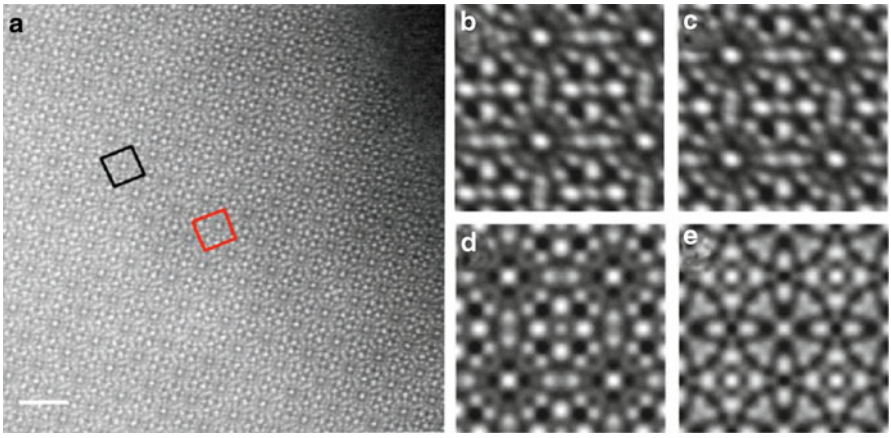

Fig. 6 (**a**) Z-Contrast image of the K_8Si_{46} clathrate, (**b**) reconstructed image using parameters from Figs. 1 and 2, (**c**) reconstructed image after shifting phases, (**d**) reconstructed image after imposing the correct *p*4*mm* symmetry and (**e**) reconstruction with incorrect phase offset

found locations and expected locations for individual unit cells. For clarity, the vectors have been magnified by a factor of 10 as within the region of the crystal the vectors are very small and point in similar directions. The vectors associated with noise (the unit cell locations marked by very small points in Fig. 5a) are much larger and random compared to their neighbors. Figure 5c shows the full reciprocal space lattice shown only partially in Fig. 4c and maps structure factor IQ (a measure of local S/N) to location on the lattice. Larger boxes mark higher local S/N and reflections with the highest S/N (lowest IQ) cluster near the origin of the FFT.

The analysis described above essentially allows us to identify and "correct" some of the artifacts in the image and to quantify the details in the image. In Fig. 6a, which again shows a [001] zone axis view of the structure, the outline of the central unit cell is marked using red lines. A second repeating motif is marked with black lines. Both the red and black lines delineate motifs that use identical unit cell vectors but differ with regard to the central atom of the unit cell (phase origins in Fourier space). Figure 6b shows a 2×2 array of unit cells generated by crystallographic methods using the structure factors extracted from the image in Fig. 6a after two cycles of unbending (following the method in Figs. 4 and 5). Figure 6c shows the same 2×2 array of unit cells after phase shifting the unit cell origin so that the expected *p*4*mm* symmetry is best obeyed. Figure 6d shows a 2×2 array of unit cells generated by crystallographic methods after enforcing *p*4*mm* symmetry. This involves forcing all the phases to be either 0 or 180° and averaging symmetry-related reflections. Figure 6e shows the incorrect result of enforcing *p*4*mm* symmetry without phase shifting the structure factor data to the correct phase origin—i.e., we can clearly identify and impose the correct symmetry on the image. The summation of all these steps is that the effects of low signal to noise on images can be accounted for and high quality images can be obtained where the contributions to contrast can be quantified.

These methods have been successfully used to quantify site occupancy in clathrates through direct comparison to Z-contrast image simulations [65]—this involves simulating the image and comparing the results to the processed images. Through such methods, high-resolution images can be obtained under a variety of conditions so that the effect of the beam on the sample can be easily identified. Furthermore, the structure that is determined under the varying conditions can be statistically defined—the number of images needed to obtain a given structure converged to a particular resolution under a given set of beam conditions. With data in this form, any statistical variability in the structure/composition can focus on understanding the synthesis rather than the experimental measurement.

3.2 Nitrogen Doping in GaAs

Another area where aberration correctors can make a large impact is the analysis of a distribution of diffuse point defects across an extended sample. To demonstrate this, a systematic study of nitrogen-doped GaAs samples was undertaken [67]. Figure 7 shows a series of Z-contrast images from four groups of three GaAsN quantum wells grown between GaAs barriers by molecular beam epitaxy (MBE), each group with different N compositions (0.1%, 0.4%, 1%, and 2.5%). The N composition was controlled by monitoring the optical intensity of the atomic N plasma emission during growth. As with the results on the clathrates, the high-resolution HAADF–STEM study was performed using a Nion aberration-corrected VGHB501-dedicated STEM operated at 100 kV with a nominal probe size of 0.1 nm.

The initial HAADF–STEM analysis of the GaAsN QWs at low magnification led to an interesting result. As can be observed in the inset in Fig. 7a, the $GaAsN_{0.025}$ quantum wells appear brighter than the GaAs barriers when imaged in HAADF–STEM despite the reduced average atomic number. As pointed by early studies by Perovic et al. [68] and Treacy et al. [69] and more recently by Grillo et al. [70], the local distortion of the lattice plays a major role in HAADF–STEM imaging of nonperfect crystals. Thus, the origin of the observed contrast may rely on the local distortion of the lattice due to the introduction of N, as pointed by Wu et al [71]. As we can see from Fig. 7a, the evolution of contrast with the N content does not follow a linear behavior; the slope of the curve for low N concentration is relatively large and for the higher N content the curve levels off. The origin of this change in contrast with %N is not immediately clear for what is supposed to be a random substitutional alloy (note that the contrast behavior is similar for a wide range of detector angles, suggesting that it is an intrinsic function of the material rather than a unique experimental condition that causes this contrast).

To investigate the origin of the observed evolution of contrast with %N, higher resolution images were obtained (Fig. 7b). For each high resolution image, the

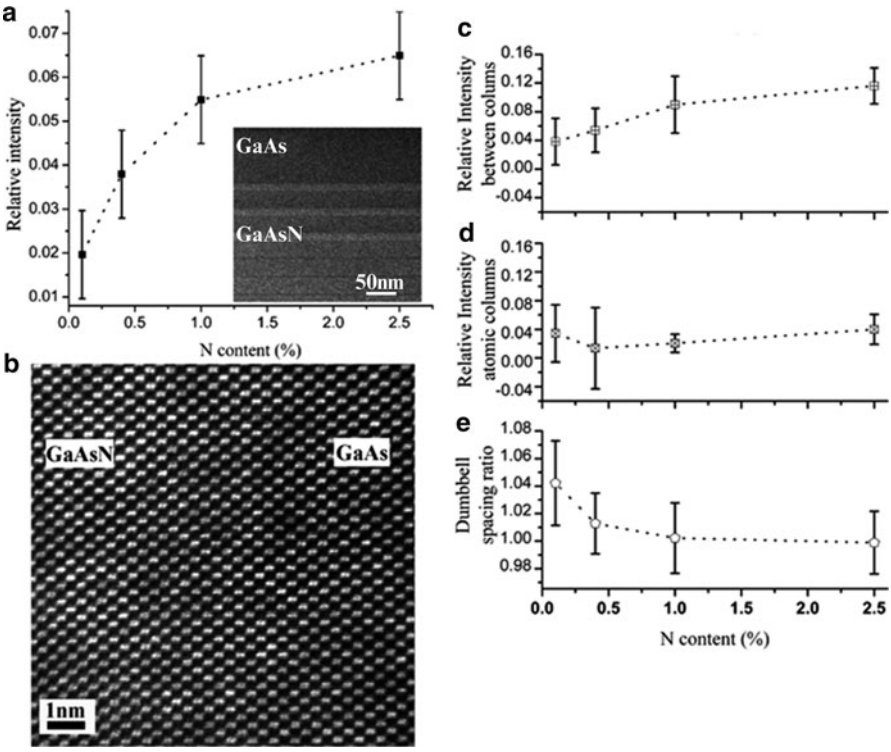

Fig. 7 (**a**) Z-Contrast image intensity increases as a function of N concentration, (**b**) high resolution Z-contrast image for the 2.5% doping case, (**c**) image contrast on the columns, (**d**) image contrast between the columns, (**e**) average dumbbell spacing

contrast from the valley between the atomic columns and from the atomic columns is plotted *vs.* %N in Fig. 7c and d, respectively. The intensity valley/peak has been measured individually for each dumbbell in each image for up to 6 images per concentration; the error bars correspond to the standard error over all these measurements (this measurement makes use of the fact that there are hundreds of dumbbells in each high resolution image). As can be clearly seen, the contrast from the valleys between columns shows a strong increase and then flattens off for higher N concentration, similar to the behavior obtained from the low magnification images, whereas the increase in contrast from the atomic columns is negligible. This reveals that the increased intensity found in GaAsN originates specifically from the valleys between the atomic columns rather than from the columns themselves. Additionally, the average dumbbell spacing was measured from the images, finding a nonlinear reduction with increasing N content (Fig. 7e). This behavior is likely caused by the incorporation of N introducing an additional strain component in the lattice.

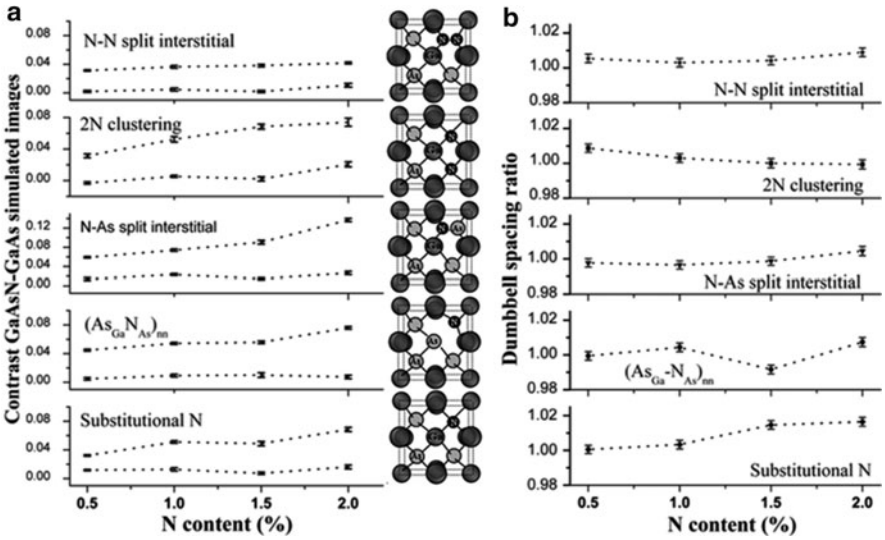

Fig. 8 (**a**) Plot of the contrast *vs*. N content from the simulated images of the different complexes, where *open symbols* correspond to the valley between the columns and solid symbols to the atomic columns; a schematic picture of each complex is included where the dark atoms represent N, the *dark grey* Ga and the *light grey* As; (**b**) averaged dumbbell spacing ratio measured from the simulated images

In order to interpret the experimental results [67], a series of possible defect structures was simulated by density functional theory and then image calculations were performed using a multislice code [72]. Figure 8 shows a summary of the results for the possible defect configurations in GaAsN. As can be seen from Fig. 8, the 2N substitutional complex is the only one for which the simulations agree with the experimental results. These results clearly point to the absence of interstitials in the alloy and to the onset of N clustering. Substitutional N pairing with up to four neighbor positions in $GaAs_{1-x}N_x$ alloys with $x < 0.025$ has been reported previously, in good agreement with these experimental observations [73]. The important aspect of these results is that by using the small variations that occur across the image (again, there are hundreds of GaAs dumbbells per image) highly quantitative analyses of images can deduce the effect of diffuse point defects on the overall structure. This type of defect analysis can of course be coupled with the image processing techniques demonstrated for the clathrates in the previous section. The key aspect of such an analysis is that the processing techniques can remove image to image variability caused by the experimental parameters, and allow us to define a structure with confidence limits and compare directly many different measurements.

3.3 *Structure/Composition Fluctuations at Dislocations in* $SrTiO_3$

Grain boundaries have long been known to have far-reaching effects on the bulk properties of perovskite materials. Notable examples include the critical currents in high-T_c superconductors ($YBa_2Cu_3O_7$) [74, 75], enhancement of the magnetoresistance effect in the manganates ($La_{1-x}Ca_xMnO_3$, $SrCaMnO_3$, etc.) [76, 77], and increases in the dielectric constant in $BaTiO_3$ and $SrTiO_3$ [78]. For perovskites, the deviation of the grain boundary atomic structure with respect to the bulk typically induces a grain boundary potential, through which the bulk properties are influenced. Accurate determination of what causes the boundary potentials is extremely advantageous to current materials, and thus a clear understanding of the atomic arrangements at dislocation cores—one of the key building blocks of grain boundaries—is essential. A complete knowledge of the dislocation core structure is a necessary component for understanding the mechanics of grain boundary doping—a powerful method to alter or control the influence of the grain boundary on the bulk properties. The importance of the grain boundary plane in controlling the properties of perovskites (and in particular $SrTiO_3$) has led to many studies by TEM and STEM over the last 20 years [79–85].

The basis for understanding the structure of [001] tilt grain boundaries in $SrTiO_3$ is the structural unit model proposed by Sutton [86] and expanded further by STEM studies in the mid-1990s [87–90]. The basic principle of the structural unit model is that the atoms in a dislocation core will arrange themselves into a repeating "structural unit." Any grain boundary that forms will then be composed of a sequence of these structural units with a distribution that correlates directly with the expected dislocation core spacing from Frank's rule [91] along the grain boundary plane (Fig. 9). The structural unit model provides an identical description of the grain boundary plane as is obtained from dislocation core models that use the burgers vector of the dislocation to define the spacing and energy of the boundary. The difference is that the structural unit model focuses on the atomic structure of the cores rather than the strain fields associated with them. As such, the structural unit model allows the presence of a sublattice to be incorporated into any model that interprets properties and there is a seamless transition from low-angle grain boundaries to high-angle grain boundaries. The initial analysis of structural units obtained from nonaberration-corrected microscopes allowed models for grain boundaries that incorporated partially occupied columns [87–90], and later oxygen vacancies [92–94] and the presence of dopant atoms on sites determined by the local strain at the grain boundary rather than the bulk defect chemistry [50]. However, while the structural units that were observed at [001] tilt grain boundaries always appeared to have the same structure, there was a large variability in the bond lengths and the apparent composition of the cores. Unfortunately, given the resolution and lack of stability of the nonaberration-corrected instruments it was difficult to see all of the atoms in the cores and impossible to quantify the contrast variations

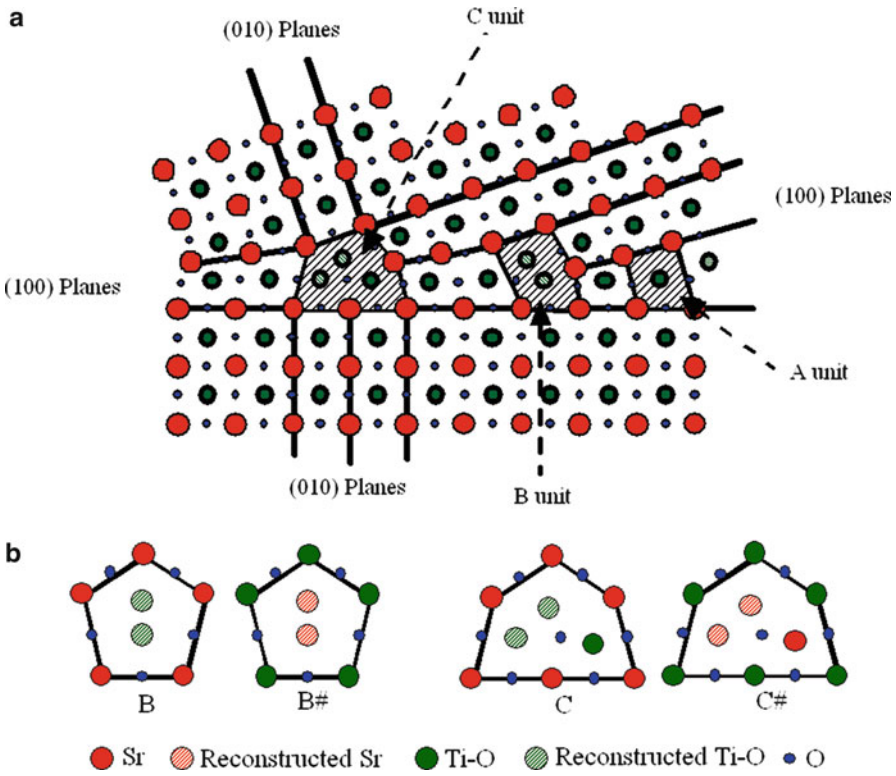

Fig. 9 (**a**) Schematic of an asymmetric [001] tilt grain boundary In $SrTiO_3$ showing the structural units as dislocation cores and (**b**) the structural units necessary to make up all [001] tilt grain boundaries from 0–90° on both sub-lattices

(i.e., composition changes) on the required atomic scale. Nevertheless, the model structures allowed the effects of grain boundary chemistry to be predicted.

The success of the structural unit model in describing grain boundaries in $SrTiO_3$ led to a 6° low-angle [001] tilt grain boundary being used as one of the first test specimens for the FEI 80–300 kV double corrected and monochromated Titan at LLNL [95]. Here the main aim of the test was not resolution (the important spacing for images is $\sim$0.27 nm and probe size in the Titan is $\sim$0.1 nm), but rather to see the level of contrast and sensitivity that could be achieved with an aberration-corrected instrument. With the advances in specimen preparation technology, the increased signal to noise in the images and the improved stability of the microscope, many images were obtained from the grain boundary plane that highlighted the core structure. From a single day's analysis, images containing 167 dislocation cores were obtained. These cores showed a high degree of variability from the simple structural unit model described above (which may be due only to the ability to see the structure more clearly with the aberration-corrected microscope or may also be due to the method of grain boundary synthesis).

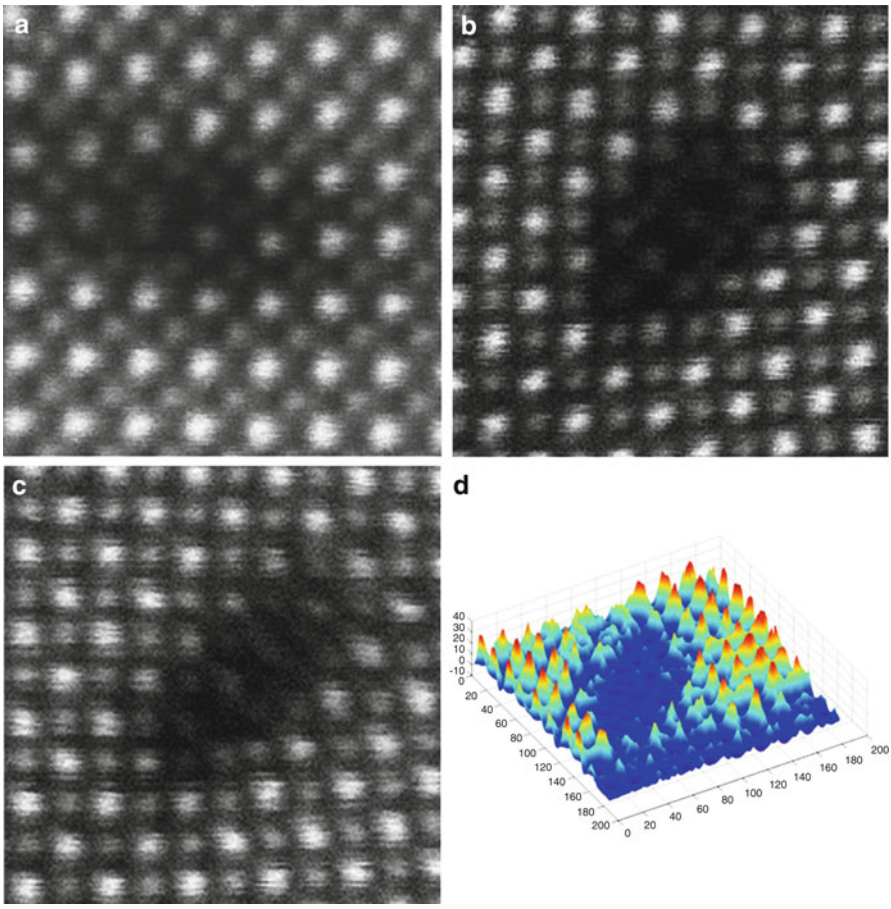

Fig. 10 Z-Contrast images of (**a**) the elongated core, (**b**) the composite core and (**c**) the transformed core (spacing between the brightest spots in the image is the Sr sub-lattice ~ 0.4 nm). (**d**) Probability density map of the sum of 167 cores showing the potential for variability in the core region

The three types of dislocation cores shown in Fig. 10 (which occur in addition to the standard structural unit cores) are referred to as elongated, composite, and transformed. The elongated core appears in both a Sr- and Ti-rich variety and is marked by the splitting of the column closest to the usual reconstructed columns seen in the structural units—elongating the core. The composite core has the termination of (100) planes in different places on the two sublattices making it a composite structural unit of both sublattices. This core structure is reminiscent of partial dislocations but there is no stacking fault separating them. The transformed core is the most surprising, containing closely packed Ti columns (confirmed by EELS) closer to a TiO_2 arrangement than a $SrTiO_3$ arrangement of

atoms. A clear reason for the differences in structure is the composition variation between the cores. The effect of the composition on the structure is represented by the probability density map which shows the probability of finding an atom in the "average" core structure. As can be seen from the core region, the density map is fairly flat indicating that there is a high degree of variability in the core that can potentially be manipulated through doping/processing to form either one of the three observed structures or a new structure.

The variability in the core structures observed here has potential implications for many aspects of the properties of grain boundaries. Typically for electroceramics, the electronic and ionic properties of grain boundaries are controlled by the composition of the grain boundary core. The results here show that variability exists in the pristine structure even before you try and dope the grain boundary to modify the properties. Future work in this area will move toward quantifying the numbers of each type of core that are present, and defining their locations along the grain boundary plane—by a detailed statistical analysis of thousands of cores it may be possible to tailor a processing step that addresses the worst/best core for a given materials property.

3.4 Size Distribution in Catalytic Nanoparticles

Catalysis is the key to controlling chemical change. It is the enabling technology of chemical manufacture, energy conversion, and much of green chemistry via pollution avoidance and pollution abatement. More than 60% of the industrial products and 90% of the processes involving chemical change are based on catalysis, and innovations are increasingly reliant on catalysis [96–98]. Many important catalysts are metals, and the most useful of them are dispersed on high-area supports. As supported metal particles are made smaller and smaller into the nanoscale regime, their properties deviate more and more from those of the bulk, and they offer new opportunities attributed to both size and support effects. To understand the properties of nanoscale catalysts the most important factor that must be characterized by STEM is therefore the size of the nanoclusters. Quantifying the size of nanoclusters seems like a trivial proposition for a microscope with $\sim$0.05 nm resolution, particularly when the typical heterogeneous catalyst system consists of heavy metal nanoclusters on a light support (very good for Z-contrast imaging). However, the issue with the nanoclusters is that they tend to move across the surface of the support under the influence of the beam. The more intense the beam gets through the use of aberration correctors, the more likely it is that the metal clusters will move [99]. Hence, as with the previous examples, we would like to have the resolution of the aberration corrector but with significantly lower beam current—leading to poorer signal to noise in the images and increased error bars in particle size measurements.

To generate an accurate measurement, σ_{meas}, of nanocluster sizes, a general mathematical formalism involving a convolution-blurring/curve-fitting algorithm has been developed [100,101]. For this method, we assume that we have a Z-contrast

STEM image with identifiable bright spots representing isolated small atomic clusters on a relatively slowly varying background (support), and that the clusters are drawn from a statistical distribution of perhaps a few different sizes and shapes. What we need to be able to generate is a precise measurement of the size of each kind of cluster, as well as an ability to distinguish various clusters on the basis of their size in order to produce population statistics of the various species present. To do this, we curve fit each particle image with a Gaussian peak plus a polynomial background to extract an estimate of its root-mean-square radius r_{RMS} (as well as its total "mass," which can also be used to help classify particles into species). This initial estimate may be subject to bias arising from the background signal, from random noise peaks, from the fact that the particle itself is not a Gaussian distribution of mass density, and from various point spread functions that blur the image. In order to try to average out the effects of some of these biases, we deliberately blur the image—digitally—using a Gaussian kernel with width σ_{gb}. Small values of σ_{gb} may be more prone to random noise spikes and limited quality of the curve fit, whereas larger values may be more influenced by effects from the background and, eventually, from the fact that the measured size will be dominated by the blur. A curve fit of the extracted r_{RMS}^2 versus σ_{gb}^2 results in an estimate of what would have been measured in a noise-free measurement with zero artificial blurring. This measurement is further corrected for systematic effects arising from the known point spread function including contributions from the probe size, vibrations, and focus errors [101]. Focus errors in particular are minimized by taking a through-focus series and analyzing, for each particle, its image at the focus value for which it appeared smallest.

We used the method described above to analyze images of MgO-supported decaosmium carbido carbonyl clusters, $[Os_{10}C(CO)_{24}]^{2-}$, formed by the reaction of triosmium carbonyl precursors, $Os_3(CO)_{12}$, in the presence of CO. Osmium in various forms is a catalyst for various conversions of hydrocarbons, including alkene hydrogenation [102]. MgO-supported osmium carbonyl clusters were chosen because; (1) osmium clusters of various nuclearities (such as 3, 5, and 10 atoms) can be synthesized uniformly and selectively on MgO support surfaces [103–105]. (2) the structures of $[Os_{10}C(CO)_{24}]^{2-}$ and $Os_3(CO)_{12}$ are well characterized (in the solid state by X-ray diffraction crystallography [106, 107] and on MgO surfaces by EXAFS spectroscopy and infrared spectroscopy [103–105]); and (3) the heavy Os atoms show high contrast relative to the light MgO support in HAADF imaging. The core structural models of the $[Os_{10}C(CO)_{24}]^{2-}$ and $Os_3(CO)_{12}$ clusters determined from the crystallographic data are illustrated in Fig. 11.

The RMS radii of $Os_3(CO)_{12}$ and $[Os_{10}C(CO)_{24}]^{2-}$ were calculated from the crystal structures in Fig. 11 and the electron elastic scattering cross-section database distributed by the National Institute of Standards and Technology (NIST) [109]. The resultant theoretical RMS radii of $Os_3(CO)_{12}$ and $[Os_{10}C(CO)_{24}]^{2-}$ are 0.202 and 0.295 nm, respectively. Note that the CO ligands (not shown in the figure) are significant contributors to the overall RMS radii. Figure 12a shows a raw HAADF–STEM image of the MgO-supported clusters obtained from an uncorrected JEOL 2500SE 200 kV TEM/STEM. It is very difficult to measure the cluster size from the

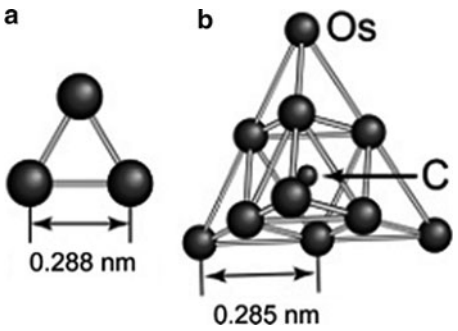

Fig. 11 Structures of (**a**) $Os_3(CO)_{12}$ and (**b**) $Os_{10}C(CO)_{24}^{2-}$ clusters from crystallographic data characterizing the compounds in the solid state combined with EXAFS and infrared data characterizing these clusters supported on MgO. The CO ligands are omitted for clarity

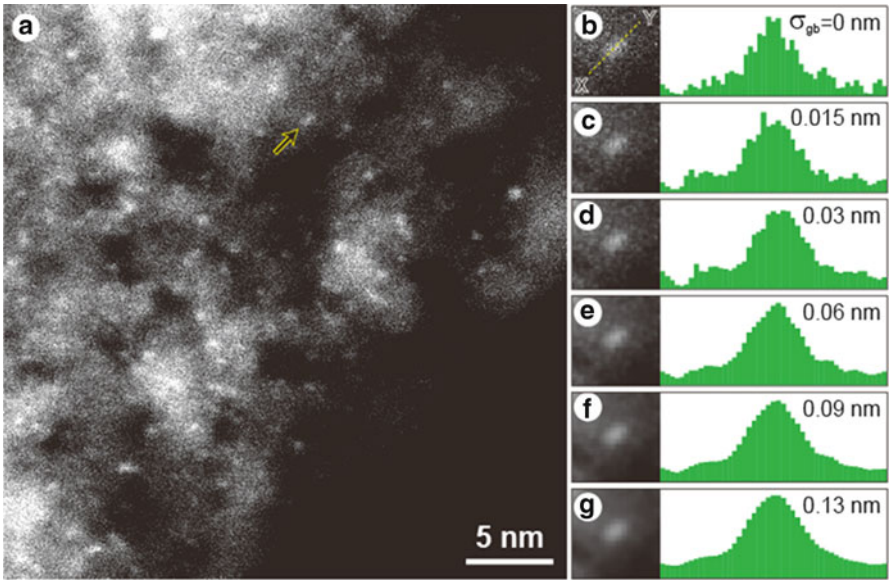

Fig. 12 (**a**) HAADF-STEM image of osmium carbonyl clusters on a MgO support. (b) Raw image of the cluster indicated by the arrow in (**a**) and intensity profile along the line X-Y. (**c**–**g**) Gaussian blurred images of (**b**) and intensity profiles. The σ_{gb} values are indicated on the top right of each profile

raw image because of the noisy intensity profile, as shown in Fig. 12b. Figure 12c–g show Gaussian blurred images and intensity profiles of the cluster indicated by the arrow in Fig. 12a. Although the noise is not completely smoothed out with small σ_{gb} values (Fig. 12c and d), it is smoothed out with larger σ_{gb} values (Fig. 12e–g).

Square regions, each including an individual cluster, were cut from the STEM images that were blurred with different σ_{gb} values. The largest clusters visible in the image were clearly too large to be single $Os_3(CO)_{12}$ or $[Os_{10}C(CO)_{24}]^{2-}$ units and were not included in the analysis. The presence of such clusters is unsurprising; these materials tend to agglomerate at the high treatment temperatures that were

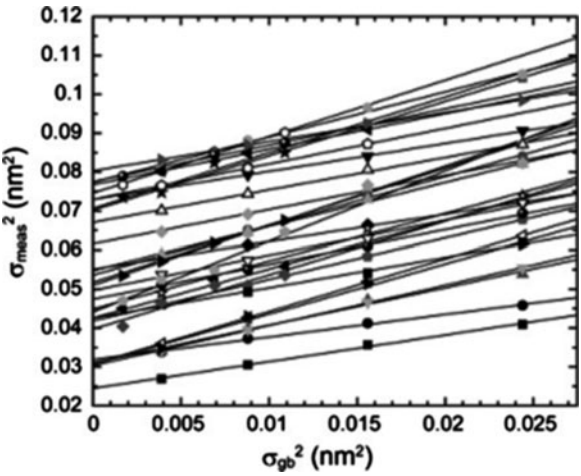

Fig. 13 The values of σ^2_{meas} characterizing 30 clusters plotted as a function of σ^2_{gb}. Lines are best fit straight lines for each cluster

used in the preparations. The threshold maximum size for accepting a cluster for analysis was deliberately set fairly high in order to ensure that all of the clearly visible, isolated $Os_3(CO)_{12}$ and $[Os_{10}C(CO)_{24}]^{2-}$ units were included. A two-dimensional Gaussian function with a planar background was fitted to the intensity profiles of the square regions to obtain standard deviations of the fitted function. The window size for the fit was about four times as large as the resultant σ_{meas} values, because neighboring clusters interfered when the window size was too large, and the background fit was not accurate when the window size was too small. The resultant σ^2_{meas} for each cluster is plotted in Fig. 13 as a function of σ^2_{gb}. By extrapolating the line back to zero in Fig. 13, we end up with a measurement of the cluster size that is independent of the blurring function (and essentially with the noise removed).

Figure 14 shows a histogram and a series of kernel density estimators (KDE) of the measured RMS radii with all known systematic effects removed for 30 clusters indicated in the STEM images. As shown by the results of Fig. 14, the clusters can be divided into three groups, designated I, II, and III, in order of size. Group I contains 6 clusters drawn from a distribution with a mean radius of 0.201 nm and a standard deviation of 0.021 nm; group II contains 14 clusters with a mean radius of 0.311 ± 0.031 nm; and group III contains 10 clusters with a mean radius of 0.416 ± 0.014 nm. These groups correspond to the $Os_3(CO)_{12}$ and $[Os_{10}C(CO)_{24}]^{2-}$ units and to positions where clusters overlap (causing the largest sizes to be observed). From these values, we may estimate *sample* standard errors *of the means* by dividing each peak's standard deviation width by $(N-1)^{1/2}$, with N being the number of clusters contributing to the peak. These values, equal to 0.009, 0.0085, and 0.0046 nm for groups I, II, and III, respectively, indicate the statistical precision to which the mean has been determined. For this sample, the mean particle sizes have therefore been determined with an accuracy better than 10 pm from a very small set of observations. The algorithm was validated and fine-tuned through

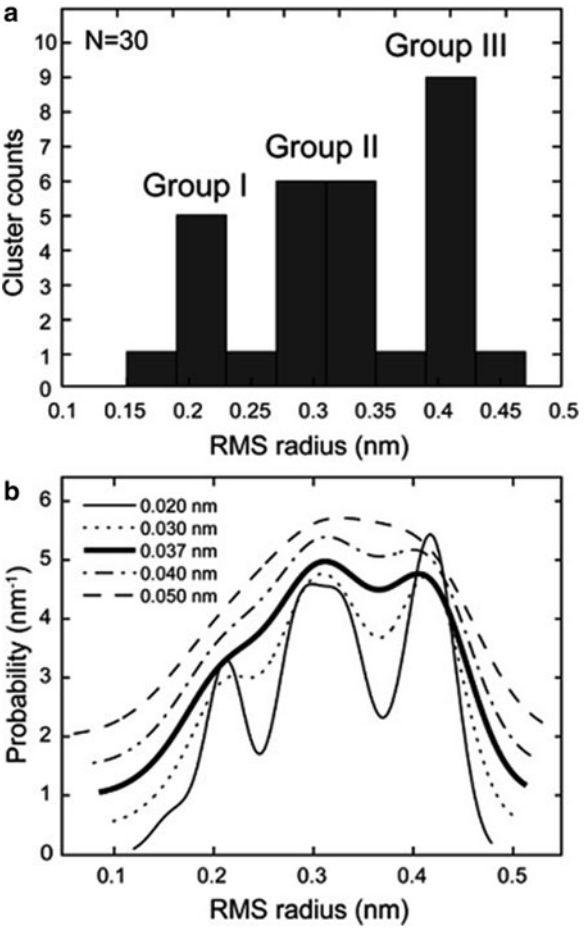

Fig. 14 Distributions of measured particle RMS radii with all known systematic effects removed. (**a**) Histogram with 0.04 nm bins and 0.01 nm offsets. Although three peaks are clearly determined for this choice, they are less clearly defined when equally valid choices are used. (**b**) Gaussian-kernel probability density estimators with varying RMS kernel width (offset for visibility); 0.037 nm is the optimum choice

computer simulation, which showed that this level of precision is what one would expect given the sample size, signal-to-noise, and signal-to-background ratios, and biases inherent in the algorithm [100]. Clearly accuracy can be increased for more observations, which will also be necessary for samples where the catalysts are not as uniform in size and shape (as is common in commercial catalysts).

4 Conclusions

The incoherent nature of Z-contrast imaging in the STEM makes it an ideal method to investigate the structure and composition of nanoscale materials, interfaces, and defects with atomic scale resolution and precision. Aberration-corrected microscopes can extend the spatial resolution into the deep subangstrom regime

for materials capable of withstanding the high-beam doses that accompany such small probe sizes. However, by controlling the beam dose and establishing the experimental parameters that allow the "optimum" dose for a particular experiment, beam-sensitive samples can also be studied with this high spatial resolution. In cases where the beam dose must be reduced, the sensitivity of the experiment may be recovered by using image processing methods. These methods are in their infancy for the study of inorganic materials, but promise to provide insights into materials properties in the future. In addition to helping the interpretation of an individual experiment, these methods allow the experimental parameters to be quantified so that comparisons can be made between experiments performed on different samples at different times using different microscopes. By making each individual experiment part of a larger set of experimental analyses, the averaging methods described in this chapter take on even more significance (as there will be more images to include in the average). Such levels of quantification should make it possible to distinguish the parameters from any experiment that are related to the experiment itself (microscope, specimen history, etc) from the parameters that are intrinsic to the materials system. Through this type of analysis, an atomic level understanding of materials properties may be possible.

Acknowledgments This work was supported in part by the U.S. Department of Energy under grant number DE-FG02–03ER46057 and by the U.S. National Science Foundation under grant number CTS-0500511. Aspects of this work were also performed under the auspices of the U.S. Department of Energy by Lawrence Livermore National Laboratory and supported by the Office of Science, Office of Basic Energy Sciences, Division of Materials Sciences and Engineering, of the U.S. Department of Energy under Contract DE-AC52–07NA27344. Experiments were also performed at two DOE user facilities: the National Center for Electron Microscopy (NCEM) at Lawrence Berkeley National Laboratory, and the SHaRE facility at Oak Ridge National Laboratory. The Clathrate work described in this paper was performed in collaboration with D. Neiner and S. M. Kauzlarich, the work on size distributions in catalysts was performed with B. C. Gates, and A. Kulkarni, the work on N-doped GaAs was performed in collaboration with D. Gonzalez, J. Pizarro, A. Yáñez, P. Galindo, R. Garcia, M.-H. Du, S.B. Zhang, and M. Hopkinson, and the work on $SrTiO_3$ grain boundaries was performed with J. P. Bradley and B. Jiang.

References

1. Hirsch PB, Horne RW, Whelan MJ (1956) Direct observation of the arrangement and motion of dislocations in aluminum. Philos Mag 1:677
2. Jia CL, Urban K (2004) Atomic resolution measurement of oxygen concentration in oxide materials. Science 303:2001–2004
3. Haider M, Uhlemann S, Schwan E, Rose H, Kabius B, Urban K (1998) Electron microscopy image enhanced. Nature 392:768–769
4. Batson PE, Dellby N, Krivanek OL (2002) Sub-angstrom resolution using aberration corrected optics. Nature 418:617–620
5. Erni R, Rossell MD, Kisielowski C, Dahmen U (2009) Atomic resolution imaging with a sub-50 pm electron probe. Phys Rev Lett 102:096101
6. Muller DA, Kourkoutis LF, Murfitt M, Song JH, Wang HY, Silcox J, Dellby N, Krivanek OL (2008) Atomic scale chemical imaging of composition and bonding by aberration corrected microscopy. Science 319:1073–1076

7. Kimoto K, Asaka T, Nagai T, Saito M, Matsui Y, Ishizuka K (2007) Element selective imaging of atomic columns in a crystal using STEM and EELS. Nature 450:702–704
8. Lazar S, Hebert C, Zandbergen HW (2004) Investigation of hexagonal and cubic GaN by high resolution EELS and DFT. Ultramicroscopy 98:249–257
9. Mitterbauer C, Kothleitner G, Grogger W, Zandbergen H, Freitag B, Tiemeijer P, Hofer F (2003) Electron energy loss near edge structures of 3d transition metal oxides recorded at high energy resolution. Ultramicroscopy 96:469–480
10. Nelayah J, Kociak M, Stephan O, de Abajo FJG, Tence M, Henrard L, Taverna D, Pastoriza-Santos I, Liz-Marzan LM, Colliex C (2007) Mapping surface plasmons on a single metallic nanoparticle. Nat Phys 3:348–353
11. Arslan I, Hyun JK, Erni R, Fairchild MN, Hersee SD, Muller DA (2009) Using electrons as a high resolution probe of optical modes in individual nanowires. Nano Lett 9:4073–4077
12. Frank J, Chiu W, Degn L (1988) The characterization of structural variations within a crystal field. Ultramicroscopy 26:345–360
13. Glaeser RM, Downing K, DeRosier D, Chiu W, Frank J (2007) Electron crystallography of biological macromolecules, Oxford University Press, New York
14. Unwin PN, Henderson R (1975) Molecular structure determination by electron microscopy of unstained crystalline specimens. J Mol Biol 94:425–440
15. van Heel M, Frank J (1981) Use of multivariate statistics in analysing the images of biological macromolecules. Ultramicroscopy 6:187–194
16. Kuhlbrandt W, Wang DN, Fujiyoshi Y (1994) Atomic model of plant light-harvesting complex by electron crystallography. Nature 367:614–621
17. Morgan D, Grant RA, Chiu W, Frank J (1992) Patch averaging of electron images of GP3*I crystals with variable thickness. J Struct Biol 108:245–256
18. Hardt S, Wang B, Schmid MF (1996) A brief description of I.C.E.: the integrated crystallographic environment. J Struct Biol 116:68–70
19. Hayward SB, Stroud RM (1981) Projected structure of purple membrane determined to 3.7 A resolution by low temperature electron microscopy. J Mol Biol 151:491–517
20. Henderson R, Baldwin JM, Ceska TA, Zemlin F, Beckmann E, Downing KH (1990) Model for the structure of bacteriorhodopsin based on high-resolution electron cryo-microscopy. J Mol Biol 213:899–929
21. Henderson R, Baldwin JM, Downing KH, Lepault J, Zemlin F (1986) Structure of purple membrane from *Halobacterium halobium*: recording, measurement and evaluation of electron micrographs at 3.5 A resolution. Ultramicroscopy 19:147–178
22. Henderson R, Glaeser RM (1985) Quantitative analysis of image contrast in electron micrographs of beam-sensitive crystals. Ultramicroscopy 16:139–150
23. Henderson R, Unwin PN (1975) Three-dimensional model of purple membrane obtained by electron microscopy. Nature 257:28–32
24. Gonen T, Sliz P, Kistler J, Cheng Y, Walz T (2004) Aquaporin-0 membrane junctions reveal the structure of a closed water pore. Nature 429:193–197
25. Crewe AV, Wall J, Langmore J (1970) Visibility of single atoms. Science 168:1338–1339
26. LeBeau JM, D'Alfonso AJ, Findlay SD, Stemmer S, Allen LJ (2009) Quantitative comparisons of contrast in experimental and simulated bright-field STEM images. Phys Rev B Condens Matter Mater Phys 80:174106
27. Pennycook SJ, Boatner LA (1988) Chemically sensitive structure-imaging with a scanning-transmission electron-microscope. Nature 336:565–567
28. Hillyard S, Loane RF, Silcox J (1993) Annular dark-field imaging—resolution and thickness effects. Ultramicroscopy 49:14–25
29. Loane RF, Xu P, Silcox J (1992) Incoherent imaging of zone axis crystals with ADF STEM. Ultramicroscopy 40:121–138
30. Amali A, Rez P (1997) Theory of lattice resolution in high-angle annular dark-field images. Microsc Microanal 3:28–46
31. Jesson DE, Pennycook SJ (1995) Incoherent imaging of crystals using thermally scattered electrons. Proc R Soc Lond A Math Phys Sci 449:273–293

32. Nellist PD, Pennycook SJ (1999) Incoherent imaging using dynamically scattered coherent electrons. Ultramicroscopy 78:111–124
33. Browning ND, Chisholm MF, Pennycook SJ (1993) Atomic resolution chemical analysis using a STEM. Nature 366:143–146
34. Browning ND, Pennycook SJ (1993) Atomic resolution spectroscopy for the microanalysis of materials. Microbeam Anal 2:81–89
35. Batson PE (1993) Simultaneous stem imaging and electron-energy-loss spectroscopy with atomic-column sensitivity. Nature 366:727–728
36. Muller DA, Tzou Y, Ray R, Silcox J (1993) Mapping SP2 and SP3 states of carbon at subnanometer spatial resolution. Nature 366:725–727
37. Duscher G, Browning ND, Pennycook SJ (1998) Atomic column resolved EELS. Physica Status Solidi 166:327–342
38. Klenov DO, Stemmer S (2006) Contributions to contrast in experimental high-angle annular dark field images. Ultramicroscopy 106:889–901
39. LeBeau JM, Findlay SD, Allen LJ, Stemmer S (2008) Quantitative atomic resolution STEM. Phys Rev Lett 100:206101
40. Findlay SD, Klenov DO, Stemmer S, Allen LJ (2008) Atomic number contrast in high angle annular dark field imaging of crystals. Mater Sci Technol 24:660–666
41. LeBeau JM, Stemmer S (2008) Experimental quantification of annular dark field images in STEM. Ultramicroscopy 108:1653–1658
42. LeBeau JM, Findlay SD, Wang XQ, Jacobson AJ, Allen LJ, Stemmer S (2009) High angle scattering of fast electrons from crystals containing heavy elements: simulation and experiment. Phys Rev B Condens Matter Mater Phys 79:214110
43. Kirkland EJ, Loane RF, Silcox J (1987) Simulation of annular dark field STEM images using a modified multislice method. Ultramicroscopy 23:77–96
44. Ishizuka K (2002) A practical approach for STEM image simulation based on the FFT multislice method. Ultramicroscopy 90:71–83
45. James EM, Browning ND (1999) Practical aspects of atomic resolution imaging and spectroscopy in STEM. Ultramicroscopy 78:125–139
46. Dellby N, Krivanek OL, Nellist PD, Batson PE, Lupini AR (2001) Progress in aberration-corrected STEM,. J Electron Microsc 50:177–185
47. Krivanek OL, Dellby N, Lupini AR (2000) Advances in Cs-corrected STEM. Proceedings of the 12th EUREM Congress, Brno **I**, 149–150
48. Krivanek OL, Nellist PD, Dellby N, Murfitt MF, Szilagyi Z (2003) Towards sub-0.5 angstrom beams. Ultramicroscopy 96:229–237
49. Xu X, Beckman SP, Specht P, Weber ER, Chrzan DC, Arslan I, Erni RP, Browning ND**,** Bleloch A, Kisielowski C (2005) Distortion and segregation in a dislocation core region with atomic resolution. Phys Rev Lett 95:145501
50. Klie RF, Buban JP, Varela M, Franceschetti A, Joos C, Zhu Y, Browning ND, Pantelides ST, Pennycook SJ (2005) A cooperative doping mechanism to enhance grain boundary transport in high-Tc superconductors. Nature 435:475–478
51. Buban JP, Matsunaga K, Chen J, Shibata N, Ching WY, Yamamoto T, Ikuhara Y (2006) Grain boundary strengthening in alumina by rare earth impurities. Science 311:212
52. Krivanek OL, Chisholm MF, Nicolosi V, Pennycook TJ, Corbin GJ, Dellby N, Murfitt MF, Own CS, Szilagyi ZS, Oxley MP, Pantelides ST, Pennycook SJ (2010) Atom-by-atom structural and chemical analysis by annular dark field microscopy. Nature 464:571–574
53. Winkelman GB, Dwyer C, Hudson TS, Nguyen-Manh D, Doblinger M, Satet RL, Hoffmann MJ, Cockayne DJH (2004) Arrangement of rare-earth elements at prismatic grain boundaries in silicon nitride. Philos Mag Lett 84:755–762
54. van Benthem K, Lupini AR, Kim M, Baik HS, Doh S, lee JH, Oxley MP, Findlay SD, Allen LJ, Luck JT, Pennycook SJ (2005) Three-dimensional imaging of individual hafnium atoms inside a semiconductor device. Appl Phys Lett 87:034104
55. Cosgriff EC, D'Alfonso AJ, Allen LJ, Findlay SD, Kirkland AI, Nellist PD (2008) 3-D imaging in double aberration corrected scanning confocal electron microscopy, Part 1: elastic scattering. Ultramicroscopy 108:1558–1566

56. D'Alfonso AJ, Cosgriff EC, Findlay SD, Behan G, Kirkland AI, Nellist PD, Allen LJ (2008) 3-D imaging in double aberration corrected scanning confocal electron microscopy, Part 2: inelastic scattering. Ultramicroscopy 108:1567–1578
57. Xin HL, Muller DA (2009) Aberration corrected ADF-STEM depth sectioning and prospects for reliable 3D imaging in S/TEM. J Electron Microsc 58:157–165
58. Arslan I, Yates TJ, Browning ND, Midgley PA (2005) Embedded nanostructures revealed in 3-D. Science 309:2195–2198
59. Arslan I, Tong J. R, Midgley P. A, Reducing the Missing Wedge: High-Resolution Dual Axis Tomography of Inorganic Materials, Ultramicroscopy 106, 994–1000 (2006)
60. Mohanty P, Ortalan V, Browning ND, Arslan I, Fei Y, Landskron K Direct formation of mesoporous coesite single crystals from periodic mesoporous silica at extreme pressure. Angew Chem (in press)
61. Evans JE, Hetherington C, Kirkland A, Stahlberg H, Browning ND (2008) Low-dose aberration corrected cryo-electron microscopy for organic specimens. Ultramicroscopy 108:1636–1644
62. Ortalan V, Uzun A, Gates BC, Browning ND Atomic-scale direct imaging of single metal atoms and metal clusters in the pores of dealuminated HY zeolite. Nat Nanotechnol (in press)
63. Buban JP, Ramasse QM, Gipson B, Browning ND, Stahlberg H (2010) Towards low-dose imaging in STEM. J Electron Microsc 59:91–102
64. Reed BW, Armstrong MR, Browning ND, Campbell GH, Evans JE, LaGrange TB, Masiel DJ (2009) The evolution of ultrafast electron microscope instrumentation. Microsc Microanal 15:272–281
65. Neiner D, Okamoto NL, Condron CL, Ramasse QM, Yu P, Browning ND, Kauzlarich SM (2007) Hydrogen encapsulation in a silicon clathrate Type I structure: $Na_{55}(H_2)_{2.15}Si_{46}$: synthesis and characterization. J Am Chem Soc 129:13857–13862
66. Morgan DG, Ramasse QM, Browning ND (2009) Application of two-dimensional crystallography and image processing to atomic resolution Z-contrast images. J Electron Microsc 58:223–244
67. Herrera M, Ramasse QM, Morgan DG, Gonzalez D, Pizarro J, Yáñez A, Galindo P, Garcia R, Du M-H, Zhang SB, Hopkinson M, Browning ND (2009) Atomic scale high-angle annular dark field STEM analysis of the N configuration in dilute nitrides of gas. Phys Rev B Condens Matter Mater Phys 80:125211
68. Perovic DD, Rossouw CJ, Howie A (1993) Imaging elastic strains in HAADF STEM. Ultramicroscopy 52:353–359
69. Treacy MMJ, Gibson JM, Short KT, Rice SB (1988) Channeling effects from impurity atoms in the HAADF of the STEM. Ultramicroscopy 26:133–142
70. Grillo V, Carlino E, Glas F (2008) Influence of the static atomic displacement on atomic resolution Z-contrast imaging. Phys Rev B Condens Matter Mater Phys 77:054103
71. Wu X, Robertson MD, Gupta JA, Baribeau JM (2008) Strain contrast of $GaNyAs_{1-y}$ ($y = 0.029$ and 0.045) epitaxial layers on (100) GaAs substrates in annular dark field images. J Phys Condens Matter 20:075215
72. Pizarro J, Galindo PL, Guerrero E, Yanez A, Guerrero MP, Rosenauer A, Sales DL, Molina SI (2008) Simulation of high angle annular dark field STEM images of large nanostructures. Appl Phys Lett 93:153107
73. Du MH, Limpijumnong S, Zhang SB (2006) Hydrogen mediated nitrogen clustering in dilute II-V nitrides. Phys Rev Lett 97:075503
74. Mannhart J, Chaudhari P, Dimos D, Tsuei CC, McGuire TR (1988) Critical currents in [001] grains and across their tilt boundaries in $YBa_2Cu_3O_7$ films. Phys Rev Lett 61:2476–2479
75. Dimos D, Chaudhari P, Mannhart J (1990) Superconducting transport-properties of grain-boundaries in $YBa_3Cu_3O_7$ bicrystals. Phys Rev B Condens Matter Mater Phys 41:4038
76. Mathur ND, Burnell G, Isaac SP, Jackson TJ, Teo BS, MacManus-Driscoll JL, Cohen LF, Evetts JE, Blamire MG (1997) Large low-field magnetoresistance in $La_{0.7}Ca_{0.3}MnO_3$ induced by artificial grain boundaries. Nature 387:266

77. Zhang N, Ding WP, Zhong W, Xing DY, Du YW (1997) Tunnel-type giant magnetoresistance in the granular perovskite $La_{0.85}Sr_{0.15}MnO_3$. Phys Rev B Condens Matter Mater Phys 56:8138
78. Heywang W (1964) Resistivity anomaly in doped barium titanate. J Am Ceram Soc 47:484
79. Kienzle O, Exner M, Ernst F (1998) Atomistic structure of $\Sigma = 3$, (111) grain boundaries in strontium titanate. Phys Status Solidi A 166:57
80. McIntyre PC (2000) Equilibrium point defect and electronic carrier distribution near interfaces in acceptor-doped strontium titanate. J Am Ceram Soc 83:1129
81. Lee SB, Sigle W, Ruhle M (2003) Faceting behavior of an asymmetric $SrTiO_3$ Sigma 5 [001] tilt grain boundary close to its defaceting transition. Acta Mater 51:4583
82. Zhang ZL, Sigle W, Phillipp F, Ruhle M (2003) Direct atom-resolved imaging of oxides and their grain boundaries. Science 302:846
83. De Souza RA, Fleig J, Maier J, Kienzle O, Zhang ZL, Sigle W, Ruhle M (2003) Electrical and structural characterization of a low-angle tilt grain boundary in iron-doped strontium titanate. J Am Ceram Soc 86:922
84. Saylor DM, El Dasher B, Sano T, Rohrer GS (2004) Distribution of grain boundaries in $SrTiO_3$ as a function of five macroscopic parameters. J Am Ceram Soc 87:670–676
85. Park MB, Shih SJ, Cockayne DJH (2007) The preferred CSL misorientation distribution in polycrystalline $SrTiO_3$. J Microsc 227:292
86. Sutton AP, Balluffi RW (1995) Interfaces in crystalline materials. Oxford University Press
87. McGibbon MM, Browning ND, Chisholm MF, McGibbon AJ, Pennycook SJ, Ravikumar V, Dravid VP (1994) Direct determination of grain boundary atomic structure in $SrTiO_3$. Science 266:102–104
88. Browning ND, Pennycook SJ, Chisholm MF, McGibbon MM, McGibbon AJ (1995) Observation of structural units at [001] symmetric tilt boundaries in $SrTiO_3$. Interface Sci 2:397–423
89. McGibbon MM, Browning ND, McGibbon AJ, Chisholm MF, Pennycook SJ (1996) Atomic structures of asymmetric [001] tilt boundaries in $srtio_3$. Philos Mag A 73:625–641
90. Browning ND, Pennycook SJ (1996) Direct experimental determination of the atomic structure at internal interfaces. J Phys D 29:1779–1794
91. Hull D, Bacon DJ (2001) Introduction to dislocations. Elsevier
92. Browning ND, Buban JP, Moltaji HO, Duscher G, Pennycook SJ, Rodrigues RP, Johnson K, Dravid VP (1999) The atomic origins of electrical barriers at grain boundaries in $SrTiO_3$. Appl Phys Lett 74:2638–2640
93. Klie RF, Browning ND (2000) Atomic scale characterization of a temperature dependence to oxygen vacancy segregation at $srtio_3$ grain boundaries. Appl Phys Lett 77:3737–3739
94. Kim M, Duscher G, Browning ND, Pennycook SJ, Sohlberg K, Pantelides ST (2001) Non-stoichiometry and the electrical activity of grain boundaries in $srtio_3$. Phys Rev Lett 86:4056–4069
95. Buban JP, Chi M, Masiel DJ, Bradley JP, Jiang B, Stahlberg H, Browning ND (2009) Structural variability of edge dislocations in a $SrTiO_3$ low-angle [001] tilt grain boundary. J Mater Res 24:2191–2199
96. Technology Vision 2020, The U.S. Chemical Industry, published by the American Chemical Society, American Institute of Chemical Engineers, the Chemical Manufacturers Association, the Council for Chemical research, and the Synthetic Organic Chemical Manufacturers Association (1996)
97. Catalysis Looks to the Future (1992) Report by panel on new directions in catalytic science and technology, Board on Chemical Sciences and Technology. National Research Council, National Academy Press, Washington
98. Critical Technologies (1992) The role of chemistry and chemical engineering, report by committee on critical technologies: the role of chemistry and chemical engineering in maintaining and strengthening american technology, board on chemical sciences and technology. National Academy Press, Washington
99. Batson PE (2008) Motion of gold atoms on carbon in aberration corrected STEM. Microsc Microanal 14:89–97

100. Reed BW, Morgan DG, Okamoto NL, Kulkarni A, Gates BC, Browning ND (2009) Validation and generalization of a method for precise size measurements of metal nanoclusters. Ultramicroscopy 110:48–60
101. Okamoto NL, Reed BW, Mehraeen S, Kulkarni A, Morgan DG, Gates BC, Browning ND (2008) Determination of nanocluster sizes from dark-field scanning transmission electron microscopy images. J Phys Chem C 112:1759–1763
102. Johansson M, Lindén AA, Bäckvall JE (2005) Osmium catalyzed dihydroxylation of alkenes by H_2O_2 in room temperature ionic liquid co-catalyzed by VO(acac)(2) or $MeReO_3$. J Organomet Chem 690:3614
103. Bhirud VA, Iddir H, Browning ND, Gates BC (2005) Intact and fragmented triosmium clusters on MgO: characterization by X-ray absorption spectroscopy and high-resolution transmission electron microscopy. J Phys Chem B 109:12738–12741
104. Lamb H. H and Gates B. C, Characterization of decaosmium carbide carbonyl clusters supported on MgO, Journal of Physical Chemistry 96, 1099–1105 (1992)
105. Allard LF, Panjabi GA, Salvi SN, Gates BC (2002) Imaging of nearly uniform Os5C clusters dispersed on MgO powder. Nano Lett 2:381–384
106. Lamb HH, Gates BC (1992) Characterization of decaosmium carbide carbonyl clusters supported on MgO. J Phys Chem 96:1099–1105
107. Jackson PF, Johnson BFG, Lewis J, Nelson WJH (1982) The synthesis of Te cluster dianion by pyrolysis—X-ray structure analysis of [N(PPH3)2]2[Os10C(CO)24] and [Os5C(CO)14H(NC5H4)]. J Chem Soc Dalton Trans 10:2099–2107
108. Corey ER, Dahl LF (1962) Molecular and crystal structure of Os3(CO)12. Inorg Chem 1:521
109. NIST Standard Reference Database 64: NIST Electron Elastic-Scattering Cross-Section Database, V. 3.1, 2003 (copyright U.S. Secretary of Commerce). http://www.nist.gov/srd/ (accessed July 4, 2007)

http://www.springer.com/978-1-4614-2190-0

Modeling Nanoscale Imaging in Electron Microscopy
Vogt, Th.; Dahmen, W.; Binev, P. (Eds.)
2012, IX, 182 p., Hardcover
ISBN: 978-1-4614-2190-0